Performance Analysis of Grid-Connected Six-Switch Current Source Inverter Under Different Switching Strategies

Kawther Ezzeddine, Mahmoud Hamouda, Hadi Y. Kanaan and Kamal Al-Haddad

October 29, 2020

Performance Analysis of Grid-Connected Six-Switch Current Source Inverter Under Different Switching Strategies

Kawther Ezzeddine[1,2], Mahmoud Hamouda[1], *Member, IEEE*, Hadi Y. Kanaan[3], *Senior Member, IEEE*, and Kamal Al-Haddad[4], *Life Fellow, IEEE*
[1]Université de Sousse, Ecole Nationale d'Ingénieurs de Sousse, LATIS-Laboratory of Advanced Technology and Intelligent Systems, 4023, Sousse, Tunisie
[2]Université de Tunis, Ecole Nationale Supérieure d'Ingénieurs de Tunis (ENSIT), 1008, Tunis, Tunisia;
[3]Saint Joseph University, Beirut, Lebanon
[4]Ecole de Technologie Supérieure (ETS), Montréal, Quebec, Canada
kawtherezzeddinee@gmail.com, mahmoudhamouda@yahoo.fr, hadi.kanaan@usj.edu.lb, kamal.al-haddad@etsmtl.ca

***Abstract*— Six-Switch current source inverter (CSI) is a promising unidirectional DC-AC power conversion topology deduced from the reversed structure of the very sparse matrix rectifier. This latter is a single-stage boost-type inverter suitable for grid-connected applications as it provides active power injection from renewable energy sources into the AC grid. This paper investigates the performance of three different soft-switching strategies for three-phase six-switch grid-connected CSI. These strategies are analyzed in terms of the number of switching transitions, DC-link current ripple, average global value of the conduction and switching power losses, as well as, the quality of the injected grid-currents. The proposed evaluation is based on both, theoretical analysis and computer simulations. A comparative study is, commonly, established and the optimum modulation strategies are selected.**

Keywords—grid-connected inverter, power quality, SVPWM, soft-switching, switching and conduction losses, PV energy.

I. INTRODUCTION

Sustainable energy (SE) sources such as photovoltaic (PV) systems, wind turbines, and fuel cells represent, nowadays, a real alternative for the traditional electrical sources. Solar energy is the finest amongst several green energetic resources; therefore, the use of PV systems for electricity generation is growing rapidly worldwide [1]. Inherently, solar modules are voltage-controlled DC-current sources. In order to, properly, inject the PV energy into the grid, a single-stage or multi-stage, power conversion system is needed. These systems have to adjust the DC-voltage across the PV generator and inject high quality AC-currents with a controllable power factor into the grid [2].

Active power injection into the grid can be achieved using two families of DC-AC power conversion topologies, namely, voltage source inverters (VSIs) and current source inverters (CSIs). Despite their effectiveness, the major disadvantage of VSIs is the utilization of bulky and defective DC-link capacitors as storage elements. Moreover, they are buck-type converters as they require a DC-link voltage higher than the peak amplitude of the line-to-line grid voltages. Consequently, a high frequency transformer or a back-to-back DC-DC converter are required to boost the DC-voltage to a desired level [3].

Several VSI topologies were proposed in the literature with the aim to, properly, interconnect the PV modules to the electrical grid. In [4]-[5], three-phase multilevel inverters were employed. Although they guarantee a proper interface between the PV panels and the grid, these structures present several disadvantages such as complex circuitry and increased number of power components, which reduces the efficiency and increases the cost of the overall system [6].

Other interesting alternatives for grid-connected applications were investigated in the literature. For example, Z-source inverters were reported in [7]-[8] specifically for residential PV systems. These inverters are a combination of a VSI and a CSI. Compared to multilevel inverters, they present a reduced number of power switches. However, they produce high input DC-current ripples, which results in high stresses on the DC-link inductors and capacitors.

On the other hand, CSIs are single-stage boost-type DC-AC power conversion topologies suitable for grid-connected applications. These latter offer several merits such as symmetric sinusoidal AC-currents at the output side of the converter, controllable power factor, fast power flow response and low voltage stresses on the switching devices [9]. Moreover, a small DC-link inductor is used as a storage element. These features make of the CSI an interesting alternative for grid-connected applications.

In [9]-[10], a CSI topology was proposed for high voltage PV systems. The switching pattern is based on a space vector with pulse width modulation (SVPWM) approach and the ON-durations of the inverter switches were calculated such that the average value of the DC-link inductor current remains constant over a switching period. A modified modulation strategy was investigated in [11] with the aim to attenuate common-mode currents. Although, a high DC-link inductance was used (i.e., 24 mH) with a switching frequency of 25 kHz, an efficiency of 97% was achieved. In [12], the one cycle control (OCC) strategy was applied for the control of the CSI. Using this strategy, the inverter preserves the advantages of simple circuitry, good stability, and fast dynamic response. Moreover, the size of the DC-link inductor is kept at low values (i.e., 0.55 mH) with a, relatively, high switching frequency of 40 kHz.

In this manuscript, the topology of six-switch boost-type grid-connected PV CSI is investigated. The control algorithm is based on the SVPWM strategy. Using this technique, a certain degree of freedom is permitted when selecting the operating regions of active and zero vectors. However, the choice of these vectors must comply with the restriction that no short- circuit at the AC-side and no open-circuit at the DC-side of the converter are allowed; a soft-switching process should be guaranteed. Moreover, the optimum modulation strategy should provide low power losses and high quality of the injected grid currents.

In the subsequent sections, three distinct, soft-switched patterns for six-switch grid-connected PV CSI are studied. The performance of these switching strategies are evaluated in terms of the number of switching transitions, DC-link inductor current ripple, global average value of conduction and switching power losses, and the harmonic component of the injected AC-currents. The analytical expressions necessary for the modulation of the proposed topology and for the description of its characteristic parameters are provided. A simulation model is, then built, to investigate the performance

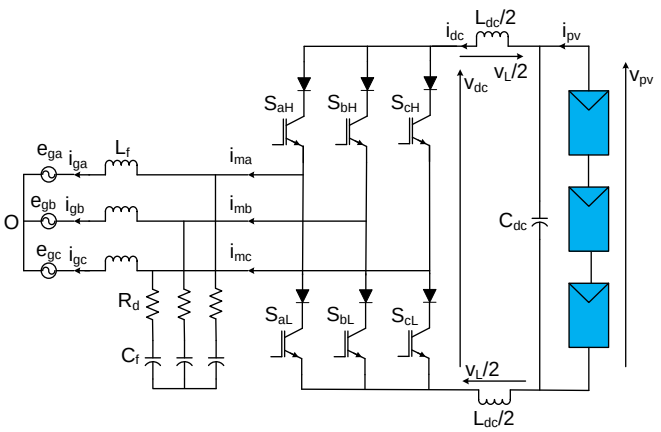

Fig. 1. Topology of Six-Switch Boost-Type Grid-Connected PV CSI

of the inverter and the obtained numerical results are presented and discussed. Based on these results the optimum strategies are selected.

II. Topology and Principle of Operation

The power circuit of the six-switch grid-connected CSI is shown in Fig.1. The latter consists of six unidirectional power switches, namely, $S_{aH}, S_{aL}, S_{bH}, S_{bL}, S_{cH}, S_{cL}$ obtained using a series combination of an IGBT and an ultrafast diode to protect the transistor against reverse voltages. A second order CL-filter (C_f, L_f) is inserted between the grid and the three AC-terminals to filter out the harmonic components in the line currents. The DC-link inductor L_{dc} acts as the instantaneous current source of the inverter used to limit the triangular ripple Δ_{Idc} of the DC-current, whereas, the ripple Δ_{Vdc} of the DC-voltage is limited with the DC-link capacitor C_{dc}.

The switching matrix of the proposed CSI is given by (1).

$$[S_{inv}] = \begin{bmatrix} S_{aH} & S_{bH} & S_{cH} \\ S_{aL} & S_{bL} & S_{cL} \end{bmatrix} \quad (1)$$

The relationships between the inverter's inputs (AC-voltages/DC-current), and outputs (DC-voltage/AC-currents) are given by equations (2) and (3), respectively.

$$v_{dc} = [S_{inv}] \begin{bmatrix} e_{ga} \\ e_{gb} \\ e_{gc} \end{bmatrix} \quad (2)$$

$$\begin{bmatrix} i_{ma} \\ i_{mb} \\ i_{mc} \end{bmatrix} = [S_{inv}]^T \begin{bmatrix} i_{dc} \\ -i_{dc} \end{bmatrix} \quad (3)$$

v_{dc} and i_{dc} are the instantaneous DC-link voltage and current, respectively. e_{ga}, e_{gb}, e_{gc} are the line-to-neutral grid voltages and i_{ma}, i_{mb}, i_{mc} are the modulated AC-currents. The grid voltages are supposed to be symmetrical and sinusoidal as given by equation (4). Moreover, the injected grid currents are required to be in-phase with their respective phase-to-neutral voltages to guarantee a unity power factor operation.

$$\begin{bmatrix} e_{ga} \\ e_{gb} \\ e_{gc} \end{bmatrix} = \hat{E} \begin{bmatrix} \cos(\omega t) \\ \cos\left(\omega t - \frac{2\pi}{3}\right) \\ \cos\left(\omega t - \frac{4\pi}{3}\right) \end{bmatrix} \quad (4)$$

$\hat{E}$ is the maximum amplitude of the line-to-neutral grid voltage and ω is its angular velocity. In the six-switch CSI topology, only one upper and one lower switch per phase-leg is switched ON at any time instant as described by equation (5) hereafter.

$$\begin{cases} S_{aH} + S_{bH} + S_{cH} = 1 \\ S_{aL} + S_{bL} + S_{cL} = 1 \end{cases} \quad (5)$$

Accordingly, for each phase-leg, there exists four distinct switching states, namely, 1, -1, 0, and X. State 1 implies that, only, the upper switch S_{iH} $(i = a, b, c)$ is switched ON. State

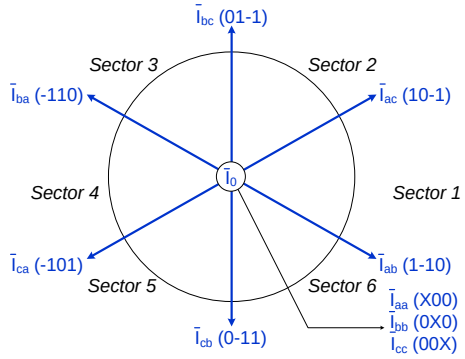

Fig. 2. Space Vector Diagram of the CSI

-1 implies that, uniquely, the lower switch S_{iL} is switched ON. State 0 implies that both switches S_{iH} and S_{iL} are switched OFF, and, State X implies that both switches along the same phase leg are switched ON. Hence, nine switching combinations are available which yield six active vectors and three zero vectors. Active vectors are obtained with the switching states 1, -1, and 0. Their amplitude is equal to $\frac{2}{\sqrt{3}} I_{dc}$ and they divide the complex plane into six sectors of 60° resulting in the space vector diagram of Fig.2. On the other hand, zero vectors are obtained when the switching state X is applied. It implies that the CSI is operating in a freewheeling mode and both switches of the same phase leg are turned ON.

III. SVPWM of Six-Switch Grid-Connected PV CSI

The CSI should provide a controlled DC-voltage at the input and impressed sinusoidal AC-currents at the output of the converter. These currents are defined as follows:

$$\begin{bmatrix} i_{ma} \\ i_{mb} \\ i_{mc} \end{bmatrix} = \hat{I}_m \begin{bmatrix} \cos(\omega t + \varphi_i) \\ \cos\left(\omega t - \frac{2\pi}{3} + \varphi_i\right) \\ \cos\left(\omega t - \frac{4\pi}{3} + \varphi_i\right) \end{bmatrix} \quad (6)$$

Where $\hat{I}_m$ is the maximum amplitude of the modulated currents and φ_i is the input displacement angle.

If the effect of the LC-output filter is neglected, the SVPWM technique synthesizes a reference current vector defined in terms of the three-phase grid-currents as follows:

$$\bar{I}_{ref} = \frac{2}{3}\left(i_{ga} + i_{gb} e^{j\frac{2\pi}{3}} + i_{gc} e^{j\frac{4\pi}{3}}\right) = \hat{I}_m e^{j(\omega t + \varphi_i)} \quad (7)$$

Depending on its location within the space vector diagram, two adjacent active vectors and one zero vector are used to synthesize the reference current vector $\bar{I}_{ref}$. For example, assume that $\bar{I}_{ref}$ is lying in sector 1 as shown in Fig.3. Here, the two active vectors $\bar{I}_{ab}$, $\bar{I}_{ac}$ and the zero vector $\bar{I}_{aa}$ are impressed with the duty cycles d_{ab}, d_{ac}, and d_{aa}.

$$\bar{I}_{ref} = d_{ab}\bar{I}_{ab} + d_{ac}\bar{I}_{ac} + d_{aa}\bar{I}_{aa} \quad (8)$$

Moreover, the following condition must be satisfied at any instant of the switching period.

$$d_{ab} + d_{ac} + d_{aa} = 1 \quad (9)$$

According to the geometrical construction of Fig.3, the following relationships are obtained.

$$\begin{cases} d_{ab}|\bar{I}_{ab}| = \sin\left(\frac{\pi}{3} - \gamma\right)|\bar{I}_{ref}| \\ d_{ac}|\bar{I}_{ac}| = \sin(\gamma)|\bar{I}_{ref}| \end{cases} \quad (10)$$

In Fig.3, $\bar{E}_g$ is the space vector corresponding to the line-to-neutral grid-voltage and $\theta = \omega t$ is its instantaneous phase angle in the complex plane. $\gamma = \theta + \frac{\pi}{6} + \varphi_i$ is the instantaneous phase angle of $\bar{I}_{ref}$ within its operating sector.

When d_{ab} is applied, the DC-current flows between the two phases a and b resulting in $|\bar{I}_{ref}| = \hat{I}_m$ and $|\bar{I}_{ab}| = I_{dc}$.

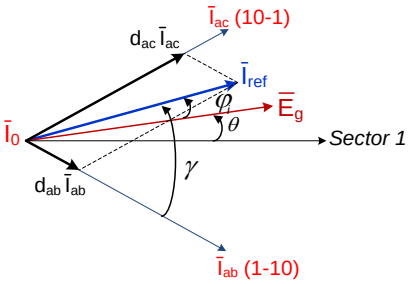

Fig. 3. Synthesis of the reference current vector within sector 1

Similarly, when $d_{ac}$is applied, we obtain $|\bar{I}_{ref}| = \hat{I}_m$ and $|\bar{I}_{ac}| = I_{dc}$. Therefore, solving (9) and (10) into d_{ab}, d_{ac}, and d_{aa} yields:

$$\begin{cases} d_{ab} = \frac{\hat{I}_m}{I_{dc}} \sin\left(\frac{\pi}{3} - \gamma\right) \\ d_{ac} = \frac{\hat{I}_m}{I_{dc}} \sin(\gamma) \\ d_{aa} = 1 - d_{ab} - d_{ac} \end{cases} \quad (11)$$

Define the modulation index m as the ratio between the amplitude of the modulated AC-currents $\hat{I}_m$ and the average DC-current I_{dc}. The maximum value of m is equal to 1 in the linear modulation region ($m_{max} = 1$).

$$m = \frac{\hat{I}_m}{I_{dc}} \quad (12)$$

The duty cycles of the CSI, in sector 1, are, finally, written as:

$$\begin{cases} d_{ab} = m \sin\left(\frac{\pi}{3} - \gamma\right) \\ d_{ac} = m \sin(\gamma) \\ d_{aa} = 1 - d_{ab} - d_{ac} \end{cases} \quad (13)$$

The preceding equations can be generalized to the six possible positions of $\bar{I}_{ref}$ by substituting the term γ with $\bar{\gamma} = \gamma - (k-1)\frac{\pi}{3}$, where k is the operating sector of $\bar{I}_{ref}$.

$$\begin{cases} d_1 = m \sin\left(\frac{\pi}{3} - \bar{\gamma}\right) \\ d_2 = m \sin(\bar{\gamma}) \\ d_0 = 1 - d_1 - d_2 \end{cases} \quad (14)$$

Furthermore, the local average value of the modulated DC-link voltage computed over a switching period can be expressed as follows:

$$\langle v_{dc} \rangle = d_{ab} e_{ab} - d_{ac} e_{ca} \quad (15)$$

Substituting (13) into (15) yields:

$$\langle v_{dc} \rangle = m \sin\left(\frac{\pi}{3} - \gamma\right) e_{ab} - m \sin(\gamma)\, e_{ca} \quad (16)$$

Finally, substituting (5) into (16) leads to:

$$\langle v_{dc} \rangle = \frac{3}{2} m \hat{E} \cos \varphi_i \quad (17)$$

Therefore, the control of the generated DC-link voltage is proportional to the variation of the modulation index m. Since $m_{max} = 1$, the maximum value of the DC-link voltage is:

$$\langle v_{dc} \rangle_{max} = \frac{3}{2} \hat{E} \cos \varphi_i \quad (18)$$

Define$\hat{E}_{L-L}$ as the peak amplitude of the line-to-line grid-voltages, such that $\hat{E}_{L-L} = \sqrt{3}\hat{E}$. Therefore,

$$\langle v_{dc} \rangle_{max} = \frac{\sqrt{3}}{2} \hat{E}_{L-L} \cos \varphi_i \quad (19)$$

This implies that the generated DC-link voltage is always inferior to the peak amplitude of the line-to-line grid-voltages. The CSI is, consequently, a boost-type (step-up) inverter [13].

IV. Switching Strategies

To synthesize the target reference vector $\bar{I}_{ref}$ and the DC-link voltage v_{dc}, a variety of switching sequences can be applied. It is, commonly, known that the double-sided symmetric patterns are superior to the single sided asymmetric ones in terms of waveform performances. Therefore, in this paper, only symmetrical sequences are investigated.

Inherently, three distinct patterns are available for six-switch grid-connected PV CSI. The possible configurations of active and zero vectors along with the voltage ($v_L = v_{pv} - v_{dc}$) and current (i_L) waveforms across the DC-link inductor for one pulse period $[0, T_{sw}]$ are illustrated in Fig.4. Here, the expected waveforms correspond to the time interval where the space vector grid-voltage $\bar{E}_g$ is located within the first half region of sector 1 (i.e.$-\frac{\pi}{6} < \theta < 0$); The line-to-line voltage e_{ab} is always greater than e_{ac}. Additionally, the DC-link inductor current and the DC-input voltage are assumed to be constant over a switching period T_{sw}.

- In strategy 1, Fig.4.a, the active switching states are placed at the beginning of the pulse half-period while only one freewheeling state is applied at the end [14].
- In strategy 2, Fig.4.b, one freewheeling state is placed at the beginning of the pulse half-period while the active states are placed at the end [15].
- In strategy 3, Fig.4.c, the freewheeling state is placed between two active switching states [16].

These strategies do not differ in terms of the number of switching transitions. Moreover, they all allow a safe commutation process of the CSI. Still, they result in different performance in terms of power losses, dc-current ripple, and the quality of the power injected into the grid.

V. Analytical Evaluation of Power Losses

Power losses of static power converters are, mainly, divided into two categories: conduction and switching losses.

A. Conduction Losses

Inherently, CSIs present high conduction losses due to the series combination of IGBTs and diodes. These latter are relatively, easy to derive regardless of the modulation strategy. According to [17], the instantaneous conduction losses($p_{c,IGBT}(t)$) of an IGBT are estimated as:

$$p_{c,IGBT}(t) = u_{CE}(t)\, i_s \quad (20)$$

$$p_{c,IGBT}(t) = U_{CE0}(t)\, i_s + r_{CE}\, {i^2}_s \quad (21)$$

i_s is the current through the device. U_{CE0} is the forward voltage drop of the IGBT and r_{CE} is its on-state resistance, assumed as constant parameters to simplify the analytical development. Therefore, the local average value of conduction losses for an IGBT ($P_{c,IGBT}$) over a grid period T_g is, given as:

$$P_{c,IGBT} = \frac{1}{T_g} \int_0^{T_g} p_{c,IGBT}(t)dt = U_{CE0}\, I_{s\_AV} + r_{CE}\, {I^2}_{s\_RMS} \quad (22)$$

Where I_{s_AV} and I_{s_RMS} are the average and RMS values of the current through the power device, respectively. Similarly, the local average value of the power conduction losses for a diode ($P_{c,diode}$) can be determined.

$$P_{c,diode} = U_F\, I_{s\_AV} + r_d\, {I^2}_{s\_RMS} \quad (23)$$

U_F and r_d are the forward voltage drop and the on-state resistance of a diode, respectively.

Thus, the local average value of power conduction losses ($P_{c,s}$) for a single switch (IGBT + diode), are given by:

$$P_{c,s} = (U_{CE0} + U_F) I_{s\_AV} + (r_{CE} + r_D) {I^2}_{s\_RMS} \quad (24)$$

The global average value of power conduction losses (P_c) of the CSI are, finally, determined by the summation of the

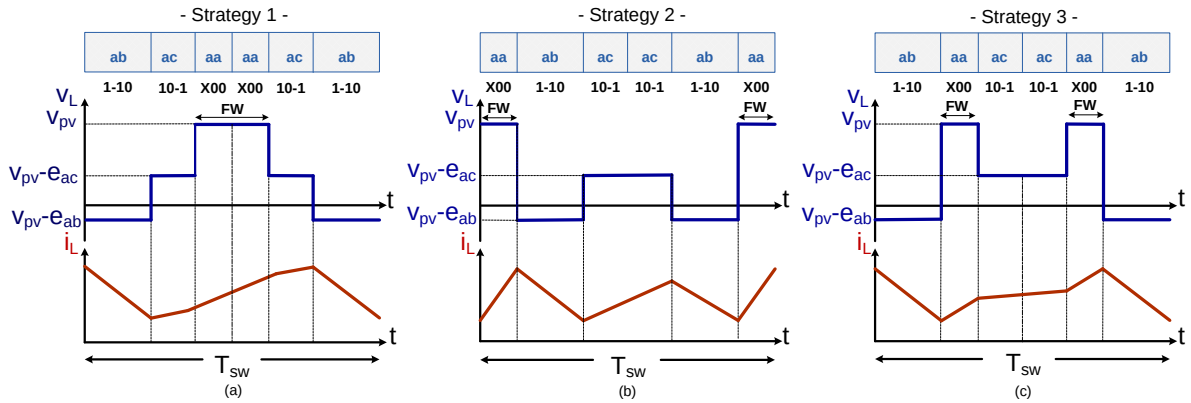

Fig. 4. Modulation strategies of CSI along with the voltage v_L across the DC-link inductor and its correspondicg current i_L; operation in sector 1 and $e_{ab} > e_{ac}$

local conduction losses $P_{c,s}$ of the power switches [13].

$$P_c = \sum_1^6 P_{c,s} \tag{25}$$

According to (24) and (25), the power conduction losses of the CSI are, mainly, dependent on the average and RMS values of the switch's current. Considering a constant dc-link current, since the conduction intervals of every power switch for all switching methods are the same, the conduction losses for all strategies would be, practically, the same.

B. Switching Losses

The global switching losses of the CSI are, strongly, related to the number of the switches' commutations over a grid period. These latter depend, in turn, on the adopted switching strategy [18]. For example, Assume that $\bar{I}_{ref}$ is located in sector 1, the freewheeling state is always obtained using the switches of phase leg a. The upper switch S_{aH} is ON state during the entire pulse period while the lower switch S_{aL} is commutating between OFF and ON states. Depending on the switching strategy, the position of the zero vector within a pulse period differs. Fig.5 shows the three possible switching patterns obtained with the proposed switching strategies for S_{aL}. The theoretical waveforms of the voltage and current across/through the switch S_{aL} (IGBT+diode) are, also, depicted. Accordingly, when modulation strategies 1 and 2 are applied, the switch S_{aL} is turned ON and OFF once per pulse period resulting in, nearly, similar switching losses. However, when considering switching strategy 3, S_{aL} commutates twice per pulse period leading to higher switching losses of the power device.

On the other hand, the switching losses of power semi-conductors are proportional to the switching current and voltage. A linearized expression of the switching loss energy of a power switch was proposed in [19] such that:

$$W_{sw} = W_{test}\,\frac{i_s}{I_{test}}\,\frac{v_s}{V_{test}} \tag{26}$$

V_{test} and I_{test} are the test voltage and current provided by the constructor's datasheet. v_s and i_s are the power semi-conductors' voltage and current at the corresponding switching instant. W_{test} is the rated switching loss energy after being turned ON and OFF once. In case of a power switch that consists of a series connection of one IGBT and one diode, W_{test} is computed as follows:

$$W_{test} = W_{ON\_IGBT} + W_{OFF\_IGBT} + W_{OFF\_diode} \tag{27}$$

$W_{ON-IGBT}$ and $W_{OFF-IGBT}$ are the IGBT's turn ON and OFF energy losses; $W_{OFF-diode}$ is the diode's turn OFF energy loss. According to Fig.5, the power switch S_{aL} can be turned ON and OFF more than one time within a pulse period (strategy 3). The switching energy losses of S_{aL} for each operating sector ($W_{sw,k}$) can be expressed in terms of the total number of operations (turn ON + turn OFF) per period ($N_{sw,k}$), the current and voltage i_s and v_s as given by equation (28).

$$W_{sw,k} = N_{sw,k}\,W_{test}\,\frac{i_s}{I_{test}}\,\frac{v_s}{V_{test}} \tag{28}$$

Moreover, within the 6 sectors of the space vector diagram, the switch S_{aL} commutates only in 3 sectors (k = 1, 3, 5). The local average value of the power switching losses of S_{aL} over a grid fundamental period can be determined as follow:

$$P_{sw,s} = \frac{3}{6}\frac{1}{T_{sw}}\underbrace{\left(W_{sw,1} + W_{sw,3} + W_{sw,5}\right)}_{W_{sw}} = \frac{1}{2}\,f_{sw}\,W_{sw} \tag{29}$$

The global average value of power switching losses (P_{sw}) of the CSI are, finally, determined by the summation of the local switching losses $P_{sw,s}$ such that:

$$P_{sw} = \sum_1^6 P_{sw,s} \tag{30}$$

The total power losses of the CSI are, finally, obtained as given by the following equation (31) [20].

$$P_{loss\_CSI} = P_c + P_{sw} \tag{31}$$

According to (29), strategy 3 will present higher switching losses and, therefore, higher total losses of the CSI as compared to strategies 1 and 2.

VI. Numerical Simulations

A numerical model was built using Matlab Simulink and tested based on the following parameters; $\hat{E} = 220\sqrt{2}$ V, $f_g = 50\ Hz$, $f_{sw} = 10\ kHz$, $m = 1$, $L_f = 2.05\ mH$, $C_f = 5.48\ \mu F$, $R_d = 2\ \Omega$, $L_{dc} = 5\ mH$ and $C_{dc} = 12.5\ \mu H$. The PV generator is emulated by a DC-voltage source with $V_{pv} = 335\ V$ and a rated DC-power $P_{dc} = 1500$ W.

Fig.6 shows the instantaneous waveforms of the DC-link current i_{dc} and the modulated voltage v_{dc} using the investigated switching strategies. As can be seen, the current i_{dc} presents a triangular ripple of amplitude ΔI_{dc} and frequency f_{sw}. It is obviously clear that the maximum amplitude of i_{dc} using all strategies is practically the same (around 5.3A). Still, strategies 1 and 2 show reduced DC-link current ripple when compared to strategy 3. These results are conform to the theoretical waveforms presented in Fig.4. On the other hand, assuming that $\bar{I}_{ref}$ is located in sector 1, v_{dc} fluctuates between the two line-to-line voltages e_{ab}, e_{ac} and zero. The application intervals of these voltages differ owing the implemented strategy and the average value of the DC-link

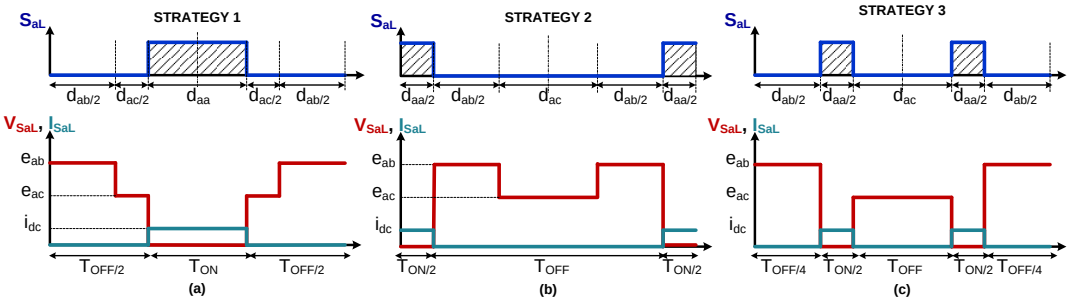

Fig. 5. Switching pattern and the corresponding voltage and current of S_aL; T_ON and T_OFF are the ON and OFF durations of the switch, respectively (Operation within sector 1 and $e_{ab} > e_{ac}$)

voltage is $\langle V_{dc} \rangle = 330\ V$ that is equal to the value expected by analytical calculations (equation 19).

The instantaneous waveforms of the voltage $v_{S_{aL}}$ across the lower switch S_{aL} of phase leg a along with its corresponding current $i_{S_{aL}}$ are illustrated in Fig.7. It is obviously clear that when modulation strategies 1 and 2 are implemented, S_{aL} commutates once per pulse-period resulting in low power switching losses (Fig.7.a and Fig.7.b). However, when modulation strategy 3 is applied S_{aL} commutates twice per-pulse period causing higher switching losses in the power semi-conductor device (Fig.7.c).

Furthermore, the injected grid current i_{ga} along the grid line-to-neutral voltage e_{ga} obtained with the three switching strategies are drawn in Fig.8. i_{ga} presents a symmetric sinusoidal outline with a peak amplitude equal to the DC-link current I_{dc}. Additionally, regardless of the switching strategy, i_{ga} and e_{ga} are practically in phase. A near-unity displacement factor operation is, therefore, achieved. Besides, the THD of the injected gird currents with an extended range of modulation index m is depicted in Fig.9. It is clear that strategies 2 and 1 provide high performance in terms of reduced grid current THD which are equal to 3.69% and 3.51 %, respectively, for m =1. The harmonic component of i_{ga} increases with the decrease of m and strategy 3 remains the worst in terms of power quality since the THD of the injected current exceeds the limits specified by grid codes, which is set to 5%, particularly, when m is below 1. The best performance of the CSI are obtained with m =1.

Finally, the power circuit was built in PLECS and a co-simulation was performed to estimate the inverter's power losses. The selected semiconductor devices are IGA30N60H3 (IGBT) and IDP30E60 (diode) of Infineon technologies. The conduction and switching power losses are, then, obtained based on the parameters provided in datasheets and the operating conditions of the inverter. The analytical and numerical results of the power losses of the CSI using the investigated switching strategies are presented in Table.1 for m = 1. According to this latter, strategies 1 and 2 present, practically, the same power losses. However, strategy 3

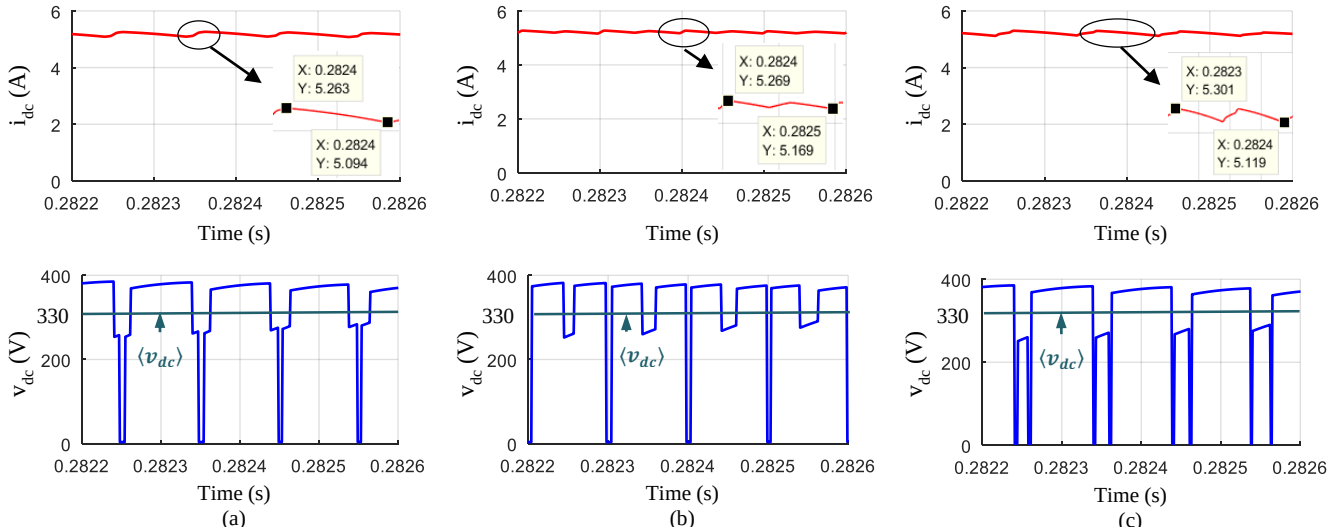

Fig. 6. Instantaneous waveforms of the DC-Link current i_{dc} and voltage v_{dc} obtained with (a) strategy 1, (b) strategy 2 and (c) strategy 3, respectively

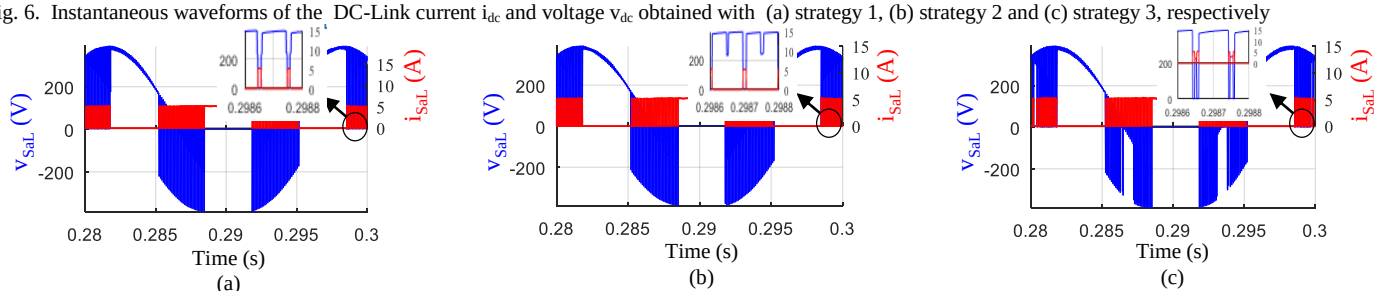

Fig. 7. Instantaneous waveforms of the switching voltage v_{SaL} across S_{aL} and its corresponding current i_{SaL} using (a) strategy 1, (b) strategy 2 and (c) strategy 3, respectively; Operation in sector 1

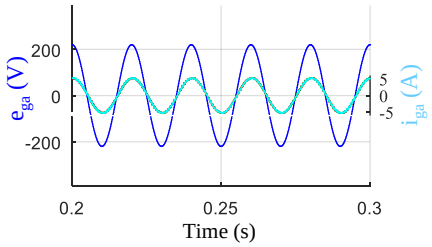

Fig. 8. Instantaneous waveforms of the grid voltage e_{ga} and current i_{ga}

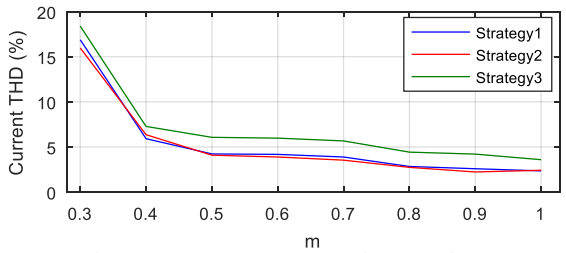

Fig. 9. THD of the injected grid currents as a function of modulation index

presents higher switching losses and, therefore, higher total losses. Consequently, the efficiency of the CSI decreases when implementing this strategy. The variation of the CSI's efficiency as a function of the modulation index m is depicted in Fig.10. Accordingly, when m decreases, the inverter's efficiency decreases while the power losses increase. The obtained results empathize the accuracy of the analytical development provided in section V

VII. Conclusions

In this paper, three different switching strategies of single-stage three-phase grid-connected PV CSI are investigated and compared to evaluate the performance of the inverter. These strategies do differ concerning the arrangement of active and freewheeling switching states. However, they all present the same number of switching transitions within a pulse period. From the obtained numerical results, the following concluding remarks are retained: Strategies 1 and 2, show the best performance in terms of a reduced DC-link current ripple and reduced switching losses. Moreover, they provide low harmonic distortion content and better quality of the injected grid currents as compared to switching strategy 3.

Therefore, the switching strategies with a freewheeling state placed at the beginning or at the end of a pulse-half period are the most appropriate for the control of grid-connected CSIs.

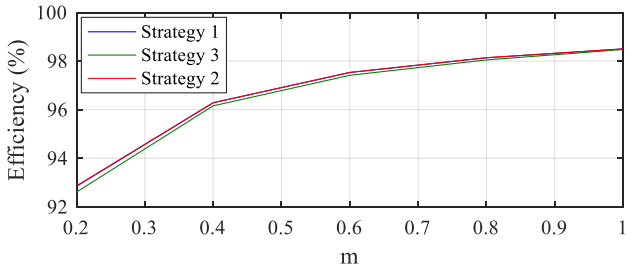

Fig. 10. Total power losses of the CSI as a function of modulation index

Table 1. Power losses of the CSI under different switching strategies

	Strategy 1	**Strategy 2**	**Strategy 3**
P_C (W)	17.7361	17.7381	17.7377
P_{sw} (W)	2.0027	1.9696	2.3166
P_{loss_CSI} (W)	19.7388	19.7077	20.0543

References

[1] B. Sahan, A. Vergara, N. Henze, A. Engler and P. Zacharias, "A single-stage PV module integrated converter based on a low power current-source inverter," IEEE Trans. Ind. Electron., vol. 55, no. 7, pp. 2602-2609, Jul. 2008.

[2] S. Alepuz, S. B. Monge, J. Bordonau, J. Gago, D. Gonzalez and J. Balcells, "Interfacing renewable energy sources to the utility grid using a three-level inverter," *IEEE Trans. Ind. Electron*., vol. 53, no. 5, pp. 1504-1511, Dec. 2006.

[3] J. A. Restrepo, J. M. Aller, J. C. Viola, A. Bueno and T. G. Habetler, "Optimum space vector computation technique for direct power control," *IEEE Trans. Power. Electron*., vol. 24, no. 6, pp. 1637-1645, Jun. 2009.

[4] F. H. Md Rafi , M. J. Hossain, G. Town and J. Lu, "Smart voltage-source inverters with a novel approach to enhance neutral-current compensation," *IEEE Trans. Ind. Electron.*, vol. 66, no. 5, pp. 3518-3529, May 2019.

[5] A. Singh, A. A. Milani and B. Mirafzal "Modified phasor pulse width modulation method for three-phase single-stage boost inverter," *in* APEC , pp. 1280, 2014.

[6] Y. Gui, X. Wang, H.Wu and F. Blaabjerg, "Voltage-modulated power control for a weak grid-connected voltage source inverters," *IEEE Trans. Power. Electron.*, vol. 34, no. 11, pp. 11383-11395, Nov. 2019.

[7] X. Zhu , B. Zhang and D. Qiu, "A High boost active switched quasi-Z-source inverter with low input current ripple," *IEEE Trans. Ind. Inform*, vol. 15, no. 9, pp. 5341-5354, Sept. 2019.

[8] K. Wolski, M. Zdanowski, and J. Rabkowski, "High-frequency SiC-based inverters with input stages based on quasi-z-source and boost topologies—Experimental comparison," *IEEE Tans. Power. Electron.*, vol. 34, no. 10, pp. 9471-9478, Oct. 2019.

[9] A. Singh and B. Mirafzal, "An efficient grid-connected three-phase single-stage boost current source inverter," *IEEE Power and Energy Technology Systems Journal*, vol. 6, no. 3, pp. 142-151, August 2019.

[10] X. Guo, N. Wang, J. Zhang, B. Wang and M. Nguyen, "A Novel Transformerless Current Source Inverter for Leakage Current Reduction," *IEEE Access*, vol. 7, no. ,pp. 50681-50690, April 2019.

[11] Y. Geng, R. Deng , W. Dong, K. Wang , H. Liu and X. Wu, "An overlap-time compensation method for current-source space-Vector PWM inverters," *IEEE Trans. Power. Electron.*, vol. 33, no. 4, pp. 3192-3203, April 2018.

[12] E. Lorenzani, F. Immovilli, G. Migliazza, M. Frigieri, C. Bianchini, and M. Davoli, "CSI7: A modified three-phase current-source inverter for modular PV applications," *IEEE Trans. Ind. Electron*., vol. 64, no. 7, pp. 5449-5459, Jul. 2017.

[13] D. Chen, J. Jiang, Y. Qiu, J. Zhang and F. Huang, "Single-stage three-phase current-source photovoltaic grid-connected inverter high voltage transmission ratio*," IEEE Trans. Ind. Electron*., vol. 32, no. 10, pp. 7591-7601, Oct 2017.

[14] B. Mirafzal, M. Saghaleini and A. Kashefi Kaviani, "An SVPWM-based switching pattern for stand-alone and grid-connected three-phase single-stage boost inverters," *IEEE Trans. Power. Electron*, vol. 26, no. 4, pp. 1102-1111, April 2011.

[15] H. Liu, y. Ran, k. Liu, W. Wang, and D. Xu, "A modified single-phase transformerless Y-source PV grid-connected inverter," *IEEE Access*, vol. 6, no. ,pp. 18561-18569, March 2019.

[16] M. Hamouda, H. F. Blanchette, K. Al-Haddad, and F. Fnaiech "An efficient DSP-FPGA-based real-time implementation method of SVM algorithms for an indirect matrix converter," *IEEE Trans. Ind. Electron.*, vol. 58, no.11, pp. 5024-5031, Jun. 2011.

[17] M. Hamouda, H. F. Blanchette, and K. Al-Haddad, "indirect matrix converters' enhanced commutation method," *IEEE Trans. Ind. Electron.*, vol. 62, no. 2, pp. 671-679, Dec. 2016.

[18] M. Mohr and F.W. Fuchs,"Comparaison of three phase current source and voltage source inverters linked with DC-DC boost converers for fuel cell generation systems," *in ECPEA*, pp. 1-10, 2006.

[19] A. Abdelhakim, P. Davari, F. Blaabjerg and P. Mattavelli, "Switching loss reduction in the three-phase quasi-z-source inverters utilizing modified space vector modulation strategies," *IEEE Trans. Power. Electron*, vol. 33, no. 5, pp. 4045-4060, May 2018.

[20] F. Schafmeister, C. Rytz and J. Kolar, "Analytical calculation of the conduction and switching losses of the conventional matrix converter and the (very) sparse matrix converter," *in* APEC, pp. 875-881, March 2005.